Atom probe tomography characterisation of powder forged connecting rods alloyed with vanadium and copper

Atom probe tomography characterisation of powder forged connecting rods alloyed with vanadium and copper

Kristina Lindgren, Karin Frisk, Maheswaran Vattur Sundaram & Mattias Thuvander

PHILOSOPHICAL MAGAZINE
https://doi.org/10.1080/14786435.2022.2089758

Taylor & Francis
Taylor & Francis Group

Atom probe tomography characterisation of powder forged connecting rods alloyed with vanadium and copper

Kristina Lindgren [a], Karin Frisk[b,c], Maheswaran Vattur Sundaram [d] and Mattias Thuvander[a]

[a]Department of Physics, Chalmers University of Technology, Göteborg, Sweden; [b]Innomat AB, Enebyberg, Sweden; [c]Department of Industrial and Materials Science, Chalmers University of Technology, Göteborg, Sweden; [d]Höganäs AB, Höganäs, Sweden

ABSTRACT

The precipitation of V and Cu in the powder forged connecting rods of Fe-V-Cu-C alloy, were studied by atom probe tomography (APT). The purpose of alloying with V was to further improve the mechanical properties of the existing powder forged materials based on Fe-Cu-C. In this study, materials tested at room temperature and 120°C were investigated. It was found that Cu was unevenly distributed on a micrometer scale. The local Cu content affected the Cu precipitation; a higher Cu content resulted in a higher volume fraction of precipitates. The V was found to form very small nitrides. The N presumably originates from the sintering process. The vanadium nitrides act as nucleation points for the Cu precipitates during cooling of the material during fabrication. APT analysis of the deformed material close to the fracture surface of the tensile test samples showed a similar volume fraction of Cu precipitates, but statistical analysis of the data indicates that both Cu and VN precipitates are more diffuse than in the undeformed material.

ARTICLE HISTORY
Received 16 March 2022
Accepted 8 June 2022

KEYWORDS
Vanadium nitride; copper precipitation; atom probe tomography; powder forging; connecting rods

1. Introduction

There is a constant drive towards increasing the performances of the internal combustion engines to meet the regulations and emission norms, by increasing the specific power output and lowering the engine displacement. Also, the trend towards hybridisation pushes for engine downsizing by moving towards increased efficiency and performance. To meet such demands of the high-performance engines, the engine components must have excellent properties to

CONTACT Kristina Lindgren kristina.lindgren@chalmers.se Department of Physics, Chalmers University of Technology, Göteborg SE-412 96, Sweden

Supplemental data for this article can be accessed online at https://doi.org/10.1080/14786435.2022.2089758

withstand such requirements [1]. Connecting rods (conrods) are high-performance components that experience high thermo-mechanical loadings. Manufacturing is performed either by drop forging of wrought steels or by powder forging. The main advantage when it comes to the powder forged conrods is the high precision from powder forging, reduced machining costs (better machinability) and the possibility to use fracture splitting [2].

The existing powder forged conrod material based on Fe-Cu-C has an excellent mechanical performance by exhibiting an enhanced strength when tested under engine operating conditions [3]. The enhanced properties at elevated testing conditions are attributed mainly to supersaturation of copper enabling fine precipitation under tested conditions. Powder forging provides a large deformation and a high density of dislocations which act as nucleation sites for Cu precipitation [3]. However, for high-performance engine applications, increasing the strength even further is of significant interest. So, the development of metal powder with vanadium as microalloying is of interest and is supposed to be competitive with the drop-forged conrods.

The term micro-alloyed or high strength low alloyed steels represent the low carbon steels with the addition of small amounts up to 0.1 wt.% of Nb, V, or Ti [4]. These alloying additions enable the formation of precipitates containing hard particles such as carbides, nitrides or carbonitrides. During austentisation, these hard particles restrict the austenite grain growth, resulting in a refined ferritic grain size upon cooling. Therefore, strengthening occurs from the grain refinement according to the Hall-Petch relation and from the precipitation of hard particles such as carbides and nitrides providing excellent toughness and increased strength levels.

It is well known that Fe-Cu alloys can be strengthened by Cu-precipitates. When studying the precipitation kinetics, it has been observed that Cu first precipitates with a bcc lattice structure, then transforms to 9R (at sizes larger than 4 nm), and finally to the fcc structure when they have grown to a large enough size [5–7]. Straining of the steel by deformation significantly accelerates the precipitation kinetics. Alloying elements that have been found to enhance Cu-precipitation are Ti, B, and Ni [8].

The precipitation of Cu in powder forged connecting rods manufactured with Fe-Cu-C powders at engine operating temperatures has been reported in several papers by Ilia et al. [9–11]. They show that on testing at temperatures of 120–150°C, Cu particles precipitate in the material. The Cu-precipitation contributes to an increase in strength at these temperatures compared to that obtained at room temperature. Deformation and the compositional inhomogeneity giving locally increased concentration of Cu in the powder forged material influence the precipitation, and can be an important advantage for powder forged material compared with wrought material.

Atom probe tomography (APT) is a characterisation technique well suited to study nanoscale precipitation, due to the 3D high resolution spatial and

chemical information gained [12]. Cu precipitation has been studied by APT in many different steel systems [13–19]. The crystallographic information gained by APT is, however, not enough to distinguish the structure of the precipitates. In this paper, APT was utilised to analyse powder forged Fe-V-Cu-C in order to gain further understanding of the nanoscale structure. The impact of V addition to this material has, to our knowledge, not been studied on the nanometre scale by APT before. In addition, transmission electron microscopy (TEM) and scanning electron microscopy (SEM) were used to characterise the material. These results are compared with calculations of phase equilibria and precipitation processes using the Thermo-Calc software package [20]. Furthermore, deformed material was analysed to see the impact of deformation on the precipitates.

2. Materials and methods

Water-atomised iron powder prealloyed with 0.12 wt.% V manufactured by Höganäs AB, Sweden, was used as a base material. It is mixed with elemental copper and graphite as a carbon source and the final composition is given in Table 1.

Conrods, see Figure 1, were manufactured by pressing the preform to 85% relative density and high temperature sintering in a nitrogen–hydrogen atmosphere, followed by subsequent forging to reach a density of 7.86 g/cm^3.

Tensile samples were machined from the I-section of the conrods according to the ASTM standard E8/8M-16A and the tensile tests were performed at elevated temperatures according to ASTM standard E21 – 09. The tensile samples can be seen in Figure 2.

For the characterisation of the deformed materials, specimens were prepared from a lightly polished cross section of the tensile specimen fracture surface. The reference material was prepared from a polished section of the tensile test shoulder of the material tested at room temperature, that is thus not deformed. The naming convention can be seen in Table 2.

In order to analyse comparable positions in terms of Cu composition, electron dispersive X-ray spectroscopy (EDX) in an FEI Quanta200 scanning electron microscope (SEM) equipped with an Oxford X-max 80 EDX detector, was used prior to the lift-out. Specimens for APT and TEM were lifted out in an FEI Versa 3D focused ion beam/scanning electron microscope (FIB/SEM). The TEM was done in an FEI Tecnai T20 microscope with a LaB_6 gun and an acceleration voltage of 200 kV. APT was performed in a LEAP 3000X HR with a

Table 1. Chemical composition of the Fe-V-Cu-C conrod utilised for investigation.

Material composition	Fe	V	Mo	Mn	Cu	C
wt.%	Bal.	0.12	0.15	0.14	3.2	0.52
at.%	Bal.	0.13	0.09	0.14	2.8	2.4

Figure 1. Photo of the connecting rod.

pulse frequency of 200 kHz, a temperature of 30 K and 0.3 nJ laser pulse energy, in order to get large analysed volumes.

The reconstruction and analysis of the APT data were done in IVAS 3.6 (Cameca), with an assumed evaporation field of 23 V/nm, image compression factor 1.65 and k-factor of 4.5. These parameters resulted in charge states in line with the Kingham curves [21], and precipitates appearing spherical. Prior to analysis of clusters, the cementite was cut away from the analyses in order to not affect the statistics. The Cu cluster number density was obtained from iso-concentration surfaces, counting edge clusters as one half. The cluster sizes were obtained from the maximum separation method (MSM) [22,23]. Cu was used as the solute atom to define the clusters. Using MSM, the parameters need to be carefully chosen [24–26] for the analyses in order to differentiate between random matrix fluctuations and real clusters, and it was found that the two analyses with the lowest Cu content required different parameters ($N_{\min}$ 18 and $d_{\max}$ 0.7 nm) than the rest ($N_{\min}$ 15 and $d_{\max}$ 0.5 nm). For the cluster sizes, the clusters were assumed to have the same structure and lattice parameter as the surrounding ferrite, and any Fe atom found inside was

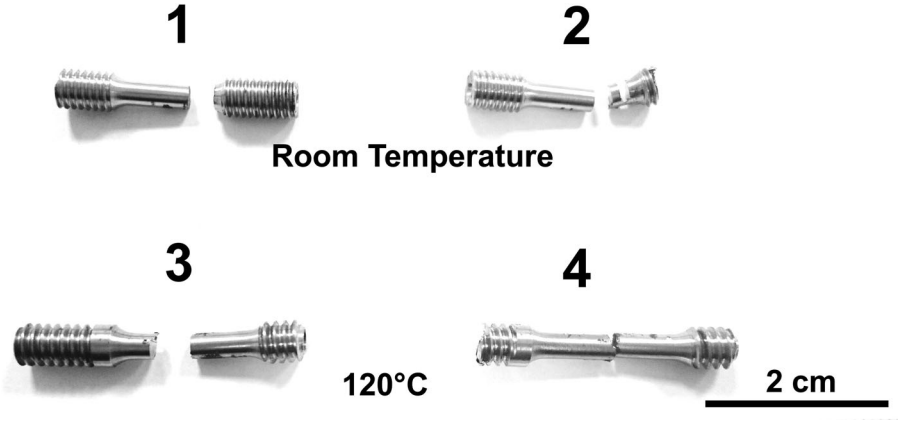

Figure 2. Tensile samples after testing. 1 and 2 were tested at room temperature, and 3 and 4 at 120°C.

Table 2. Naming of materials.

Material condition/position	Name
Undeformed (from the shoulder of the tensile specimen tested at room temperature)	M-ref
Close to fracture surface after tensile testing at room temperature	M-RT
Close to fracture surface after tensile testing at 120°C	M-120

excluded, assumed to be there due to the local magnification effects originating from the field evaporation process. Thus, it is possible that the cluster sizes are somewhat underestimated. The Cu matrix content was obtained from proximity histograms [27] based on 2.8% Cu iso-concentration surfaces. In order to avoid the higher Cu content directly outside the iso-concentration surface and depletion of Cu giving a contribution to the matrix content, distances of 3–6 nm outside of the iso-concentration surfaces were used.

Furthermore, the normalised radial distribution function (RDF) was used to analyse the APT data [28]. The RDF is the normalised average concentration of a specific element as a function of the distance to another specific element. It shows tendencies for clustering, by an increase for small distances. The RDF is a user independent method, not requiring any choice of parameters.

3. Results

3.1. Overview

The microstructure is mainly pearlitic surrounded by pro-eutectoid ferrite as shown in Figure 3. Another interesting observation is the presence of martensitic traces, mainly from the Cu supersaturation. SEM/EDX reveals large variations in Cu content on a 20 μm scale, as is expected due to Cu addition in the form of elemental Cu to the base powder during the manufacturing process, see Figure 3(c). The Cu content varies locally between roughly 0.8 and 3.5 at.% in the material.

The room temperature properties of the vanadium prealloyed material displayed an enhanced strength as compared to the Fe-Cu-C material, as seen in Table 3. At higher temperatures, the mechanical properties were inferior and to understand this behaviour, advanced characterisation is necessary, see below.

3.2. Detailed microstructure

In the TEM micrograph, thin cementite lamellae can be observed, as seen in Figure 4(a) for M-RT. The ferrite appears deformed, resulting in the varying contrast. In the micrograph, 10–30 nm Cu-particles can be seen, both in the cementite and in the cementite/ferrite boundary. These particles are also observed in all materials in the APT analyses, see Figure 4(b) for a

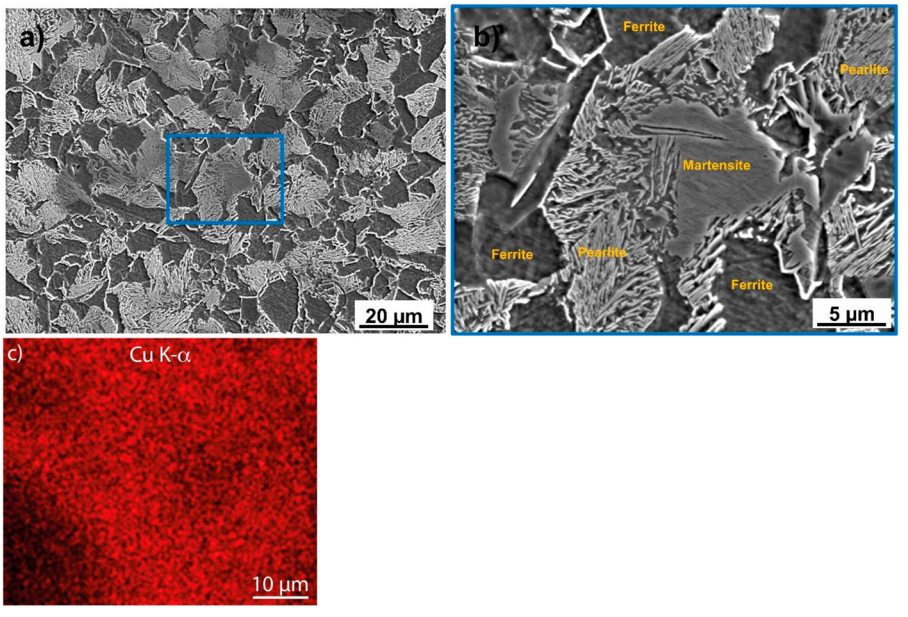

Figure 3. SEM micrograph (a) overview, and (b) enlarged view of the marked area in (a), showing a pearlitic and ferritic microstructure. In (c), a qualtitative SEM/EDX Cu-map of another area is shown, in this specific area showing Cu varying between 1.7 and 3.5 at.%.

reconstruction of M-120. In the ferrite matrix, there are smaller Cu particles or clusters observed in the APT data, that were not observed in the TEM due to their small size (resulting in coherent precipitates). The Cu particles in the ferrite were found to vary in size and number density depending on the local Cu content, as described below.

In Table 4, the average composition of the metal volumes, excluding cementite, is given, as measured by APT. The error given is the standard deviation between the analyses, and shows a significant spread in the Cu content. The Cu content is below the average Cu content of the material, due to the preferential choice of locations by EDX-mapping for the lift-outs for APT analysis, in order to get Cu contents within the same interval for all three material states. Other elements are relatively evenly distributed between APT analyses, as would be expected since they originate from the Fe powder.

Table 3. Mechanical properties of Fe-Cu-C [3] and Fe-V-Cu-C material from this study.

	Fe-Cu-C (HS170 M) From [3]		Fe-V-Cu-C Material from this study	
Testing conditions	UTS, MPa	YS, MPa	UTS, MPa	YS, MPa
RT	1202	855	1251	972
120°C	1261	900	1151	870
150°C	1240	861	1133	854

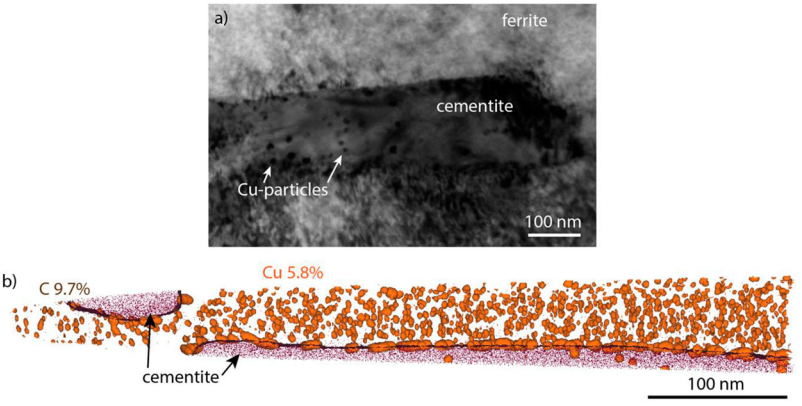

Figure 4. (a) Bright field TEM of M-RT. The deformed ferrite matrix contains cementite, and Cu-particles can be seen in the cementite and the ferrite/cementite boundary. (b) A full APT reconstruction of M-120, showing Cu particles by Cu 5.8 at.% iso-concentration surfaces (orange), and cementite by C 9.7 at.% iso-concentration surfaces (burgundy). Furthermore, some of the C atoms in the cementite are shown as dots, also in burgundy.

In Figure 5, a mass spectrum of one of the APT runs is shown. The enlarged parts of the spectrum show that Cu evaporate mainly as Cu^{+} (as is expected from the Kingham curves for an evaporation field of 23 V/nm [21]). There is a very small number of Cu atoms evaporating as Cu^{2+}, but the main contribution at mass to charge state ratio 32.5 Da is VN^{2+}, as the height of the peak does not match the natural isotopic abundance of Cu (orange dotted lines in the figure).

The Cu, V and VN (Cu^{+}, V^{2+} and VN^{2+} in the APT mass spectra) distribution in 10 nm thick slices of all analyses can be seen in Figure 6. The extent of Cu precipitation is varying within the same material condition, in terms of number density, cluster size, and how diffuse the clusters appear. The total Cu content of each analysis is also given in the figure, as it has a significant effect on the Cu precipitation.

Table 4. Average metal composition of all analyses measured by APT. The standard deviation between the 11 measurements is given as the error.

Element	Composition (at.%)
Fe	balance
Cu	1.31 ± 0.43
Mo	0.39 ± 0.13
N	0.36 ± 0.13
Mn	0.15 ± 0.01
V	0.10 ± 0.01
C	0.07 ± 0.02
Cr	0.04 ± 0.01
Al	0.03 ± 0.02
Ni	0.02 ± 0.01
Si	0.02 ± 0.01
P	0.02 ± 0.01

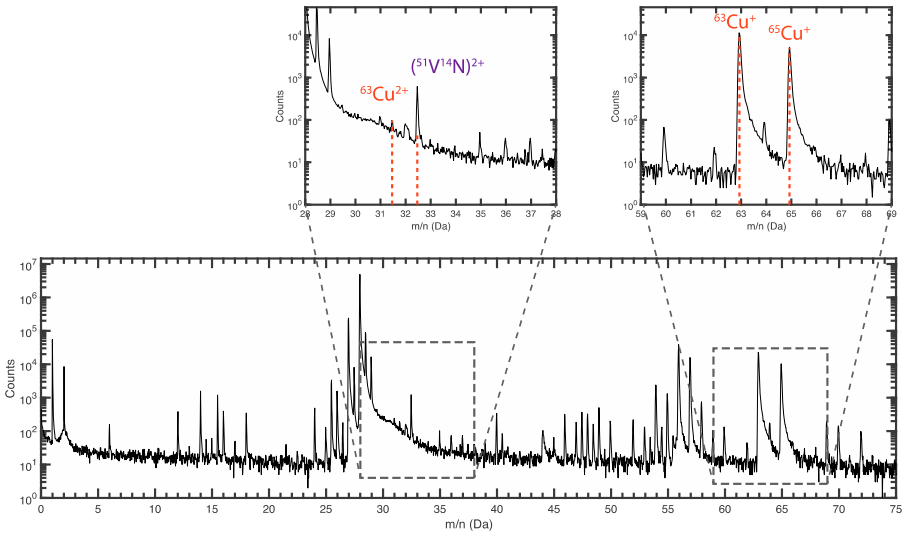

Figure 5. A representative APT mass spectrum, showing the intervals where Cu is found enlarged. The natural isotopic abundance of Cu is marked with orange dotted lines.

Furthermore, V is found to cluster. These are assumed to be (possibly sub-stochiometric) vanadium nitrides. From here on, the vanadium nitrides are denoted VN although they, according to the APT data, contain less N than V. Carbon was not found to a significant amount in these precipitates, and is located mainly in the cementite. The number density, size and how well-defined the VN clusters are varied between the different analyses.

In Figure 7, some statistics on the precipitation are presented. The Cu precipitate number density can be seen as a function of Cu content of the analysis in (a). The total Cu content is clearly affecting the number density, where a higher Cu content gives a higher number density, although M-ref spreads a lot. For the precipitate diameter (b) there is no obvious trend with Cu content. When comparing the total Cu content subtracted by the matrix Cu content (c) it can be seen that this is related to the solubility of Cu during the manufacturing, since all APT analyses end up on a single straight line. This is expected as the Cu matrix content is similar for all analyses (0.87 ± 0.14 at.% with no trends regarding material or total Cu content). This is further supported by the precipitate volume fraction that is approximately the same measure (as seen in (d)). Considering this, the Cu content affects the clustering significantly, and needs to be kept in mind when further interpreting the clustering statistics. It also tells us that the number of Cu atoms in the precipitates was not significantly influenced by the tensile testing, only by the local Cu content.

In Figure 8, the Cu-Cu RDFs for all materials are given, as well as the RDF value at zero distance as a function of the Cu content. The RDF at small distances is dependent on multiple factors; the precipitate number density, the precipitate size, and the Cu content in precipitates and in the matrix. Therefore,

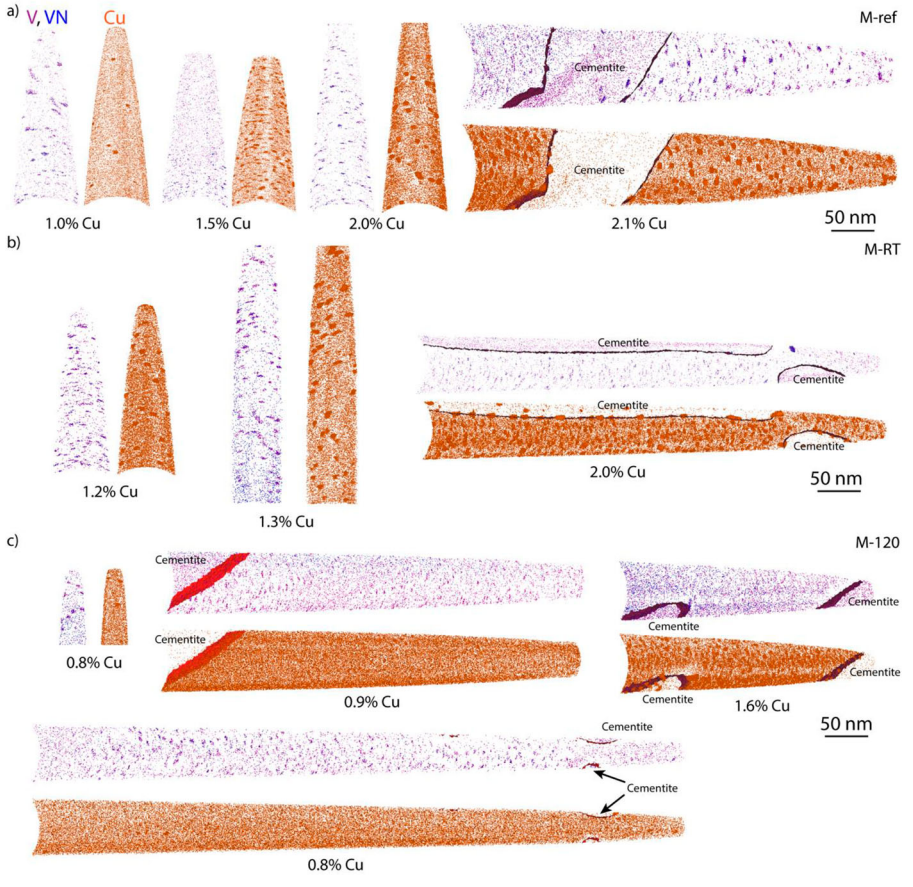

Figure 6. 10 nm thick slices showing all Cu and V + VN ions in all the APT reconstructions. All ions have the same size, and the magnification of all reconstructions is the same. The Cu content for each analysis is included. In (a), M-ref can be seen. In (b) M-RT can be seen, and in (c) M-120 can be seen.

it is expected that the RDF(0) increases with increasing Cu content, as is the case in the reference material, where a linear function has been fitted to the data points. However, in the tested materials, the same trends cannot be observed. These materials have been severely deformed during testing, and the local number of dislocations that have passed, has most probably varied significantly between different locations. A dislocation passing a precipitate would shear the precipitate, and hence make it more diffuse, something that would decrease the RDF(0) value. It is also possible that the local deformation could increase the diffusion slightly, making the Cu precipitates more diffuse without changing the precipitate volume fraction. The magnitude of the decrease would vary dependent on the very local deformation of that specific analysis volume.

The V-V RDF in Figure 9 indicates the varying extent of VN formation in the different analyses. For this plot, the VN ions were ranged as V in order to not

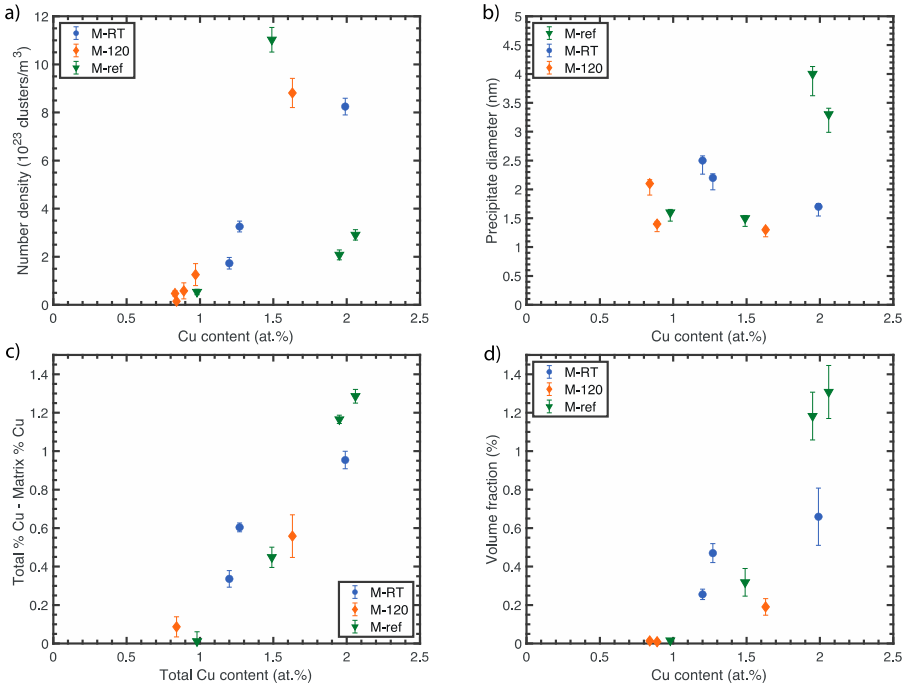

Figure 7. Cu precipitate number density, average precipitate diameter, total Cu content – matrix Cu content, and precipitate volume fraction, all given as functions of the Cu content of the analysis. The error bars are estimated from the cluster counting error in (a), from varying the MSM d_{max} parameter by 0.05 nm in (b) and (d), and from the estimated error of the Cu matrix content of each analysis in (c).

distinguish between these ions. It can be seen that the average value at zero distance is higher for the reference material than for the deformed materials, suggesting an influence from the dislocations on the VN precipitates as well.

The Cu-V RDF in Figure 9 shows a correlation between the Cu atoms and V/VN atoms, meaning that there is a possible correlation between the two types of

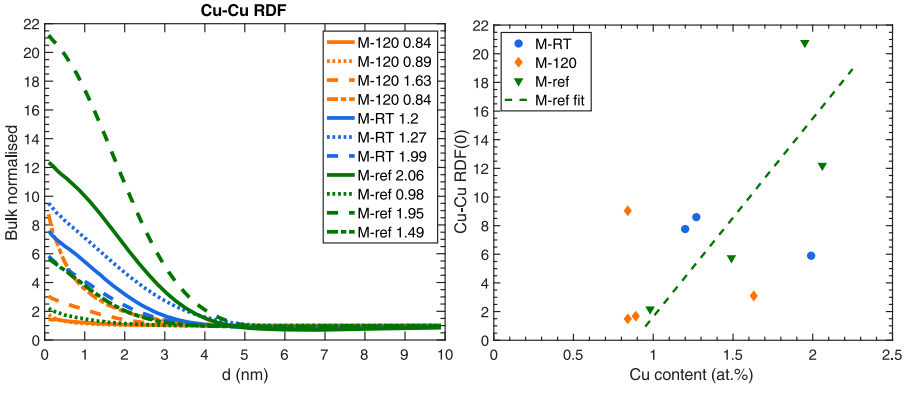

Figure 8. Normalised Cu-Cu RDF for all analyses, as well as the extrapolated Cu-Cu RDF values at d = 0 nm.

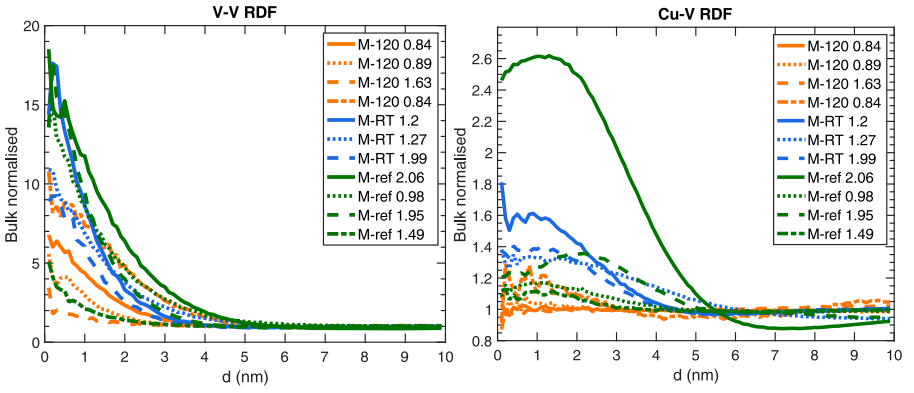

Figure 9. V-V and Cu-V RDFs for all APT analyses show the V clustering and correlation between V and Cu. VN ions are ranged as V for these plots.

precipitates. Furthermore, the maxima at 2 nm in some of the curves indicate that the precipitates are located next to each other, rather than being part of the same precipitate. Examples of this can be seen in Figure 10 where some of the Cu precipitates are located in connection to VN. Interpreting the magnitude of the RDFs shown in Figure 9 is not straightforward, as it will be affected not only by the correlation but also by the extent of clustering of Cu and V in each analysis.

3.3. Calculations of phase equilibria and precipitation kinetics

Figure 11 shows the phase equilibria in the studied material, as predicted from calculations using the Thermo-Calc software with the TCFE9 database [20]. In the solid state, at equilibrium at a temperature below the austenite to ferrite transition at around 718°C, the calculations predict that we can expect cubic V-carbides (VC) and fcc-Cu together with cementite. If nitrogen is included in the calculations, we predict precipitation of a V(C,N) phase at high temperatures. Depending on the content of nitrogen and the temperature, varying

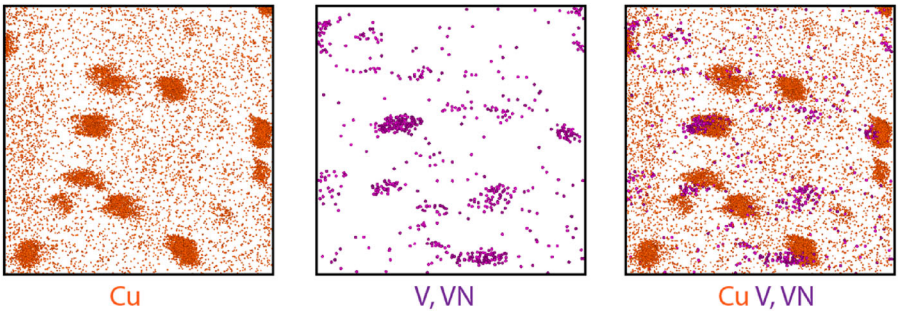

Figure 10. $50 \times 50 \times 10$ nm^3 boxes showing the Cu, V and VN distributions. The example shown is M-ref with 2.1 at.% Cu.

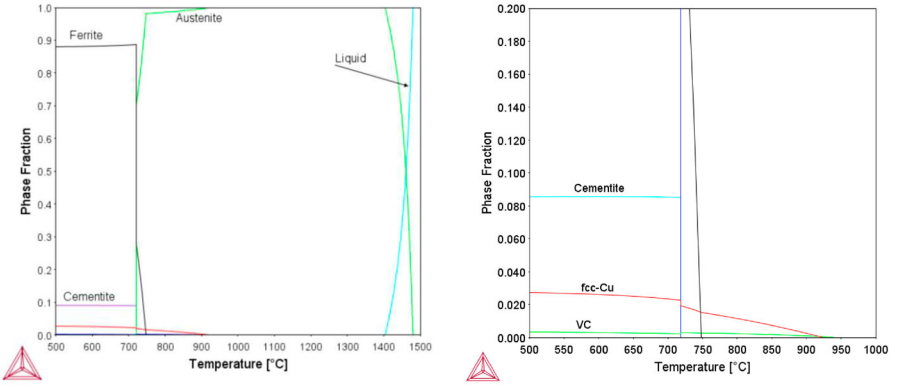

Figure 11. Calculation of the equilibrium phases in a Fe-2.8Cu0.13V-2.3C alloy.

amounts of C and N are found. At high temperatures the V(C,N) phase contains mainly nitrogen. The effect of the nitrogen content on the phase equilibria is shown in Figure 12.

The material investigated in this study is powder forged and has a complex temperature history. From the forging temperature (above 1100°C) the material is cooled in air, and it is during this cooling that precipitation of carbides, nitrides, and Cu particles is expected to take place. There is no solubility of V in fcc-Cu, or Cu in the VC, so VC and fcc-Cu will precipitate as separate phases [29,30]. Also, we have not found any evidence of solubility of Cu in V(C,N) or VN. As discussed above, there is a compositional variation of Cu and C contents in the material which will affect the fraction of precipitates locally. The calculated effect of Cu variations on the equilibrium phase fractions

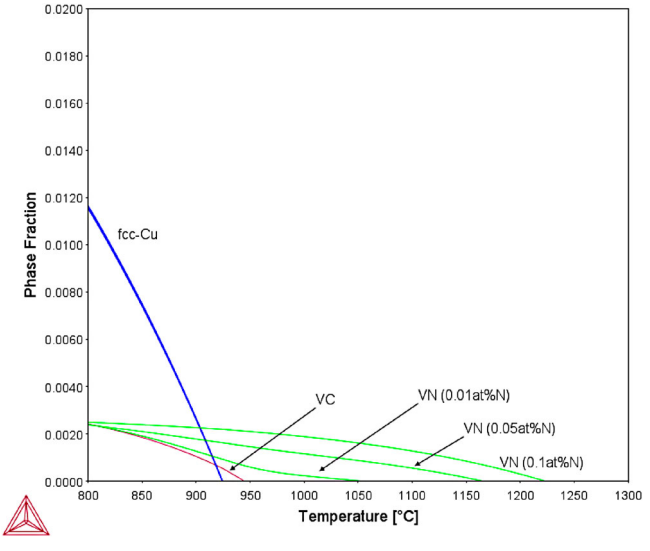

Figure 12. Calculation of equilibrium phases, with varying amounts of N.

Table 5. Effect of compositional variations on the phase fractions.

Composition Range	at% Cu	Fcc-Cu (mol%)	VC (mol%)
Low	1	0.5	0.2
Mean	2.5	2.0	0.2
High	3.0	2.5	0.2

at 700°C is listed in Table 5. Locally in the material, the C content varies between approximately 2–2.7 at%, and for the calculations 2.5 at% C was selected.

Assuming that we have a negligible nitrogen content, the precipitation of cementite, fcc-Cu, and VC was simulated using PRISMA, a module for precipitation calculations within the Thermo-Calc software. The simulations were performed for the composition 2.8 at% Cu, 2.3 at% C, 0.13 at% V. Fcc-Cu and VC were assumed to precipitate as spheres and cementite as plates, in a bcc matrix phase. The interfacial energies (cementite = 0.17, VC = 0.02, fcc-Cu = 0.48 J/m^2) and the molar volumes (cementite = 6.10^{-6}, VC = 6.10^{-6}, fcc-Cu = 7.4.10^{-6} m^3/mole) were selected from the software and database generated values, and the simplified growth model was used since we have a system with a low supersaturation [31]. The temperature profile that was applied is a slow cooling from 700°C to 600°C, in 20 min, with a slightly higher rate in the beginning. The results for the precipitate sizes are shown in Table 6 and in Figure S1 in the supplementary material. The predicted radius of the Cu precipitates is 3 nm after 20 min, in reasonable agreement with the experiments. The cementite plates have a length of close to 70 nm, with an aspect ratio of 10, which was arbitrarily selected. This predicted result is difficult to correlate with experiments other than qualitatively. However, the order of magnitude is in line with the experiments. The size of the precipitated VC carbides is very small, less than 1 nm, and as seen in Table 6 and Figure S2 and S3 in supplementary material, the VC-precipitates have a negligible volume fraction and number density.

The presence of VN that was observed experimentally can be understood by performing a precipitation simulation at higher temperatures, as shown in Table 6. Precipitation simulations at temperatures above 718°C were applied to test how VC or VN precipitate at higher temperatures, and 10 min cooling profile from 950°C to 740°C was selected for this test. VC or VN precipitation occurs at these temperatures, depending on the content of N. Both VC and VN

Table 6. The calculated number density and mean size of the precipitated phases for a specified cooling heat treatment, LT is a cooling from 718°C to 600°C in 20 min, and HT is a cooling from 950°C to 740°C in 10 min. For the fcc-Cu, VC and VN the size is the radius, and for the cementite, the size is the length.

Phase	Number Density (m^{-3})	Cooling Cycle	Mean Size/Radius (nm)
Cementite	4.1×10^{21}	LT	67
Fcc-Cu	2.3×10^{23}	LT	3
VC	3×10^{6}	LT	0.5
VC/VN	$9 \times 10^{23}/1 \times 10^{24}$	HT	0.5

are predicted in very low volume fractions (less than 0.05%) and small radii (~0.5 nm), and the number density is in a similar order of magnitude as measured.

A few different cooling profiles were tested by simulations as well as isothermal holdings at temperatures below 718°C. The results are somewhat affected by the cooling rate, but the general features remain the same. Continuing the cooling down to room temperature will not significantly affect the results, since the equilibrium phase fractions of the precipitates were reached at 600° C, and the continued coarsening at low temperatures is very slow.

4. Discussion

In this paper, powder forged Fe-V-Cu-C was studied in detail, in order to understand the impact of the addition of V, and the distribution of Cu atoms. It was found that the Cu distribution was very much affected by the varying and local Cu composition, in line with what was observed by Ilia et al. in a similar Fe-Cu-C powder forged material [3]. They did, however, not observe any Cu precipitates with 1–4 nm (diameter) size. Furthermore, the APT results on Cu precipitation and VN is qualitatively in line with the Thermo-Calc results, in terms of sizes, number densities, and volume fractions.

VN and VC have the same structure, and N and C are fully interchangeable [32]. The exact stoichiometry of these precipitates is hard to estimate due to their small size, but the APT data suggest that they are most likely somewhat sub-stoichiometric. It is however concluded that they are nitrides as seen in APT although a small amount of C could be present. The number density of VN was not estimated by APT as they are both small, diffuse, and the extent of clustering is very different in the different analyses, making comparative analysis of the data extremely hard. A possible reason for the variable VN precipitation could be the cooling rate at high temperatures that was not controlled and thus might vary slightly and impact the precipitation at these temperatures. However, the number densities are in the same order of magnitude as for the Cu precipitates, and thus they are significantly higher than the simulated number at low temperatures. The high temperature simulation thus seems more adequate for VC. The presence of VN can be understood due to the pick-up of nitrogen during sintering that was performed in nitrogen containing atmosphere [33].

It is indicated in the Thermo-Calc simulations that Cu precipitates after VC/VN, see Figure 12, and Figure S3 in the supplementary material. Thus, together with the indication of a spatial correlation between Cu and V atoms in the APT data RDF (Figure 9) that is in some cases largest at 1–3 nm, it is concluded that the VN acts as points of nucleation for the Cu precipitates. Cu precipitates have also nucleated on the matrix/cementite interface, resulting in somewhat larger precipitates than in the metal matrix, as seen in Figure 4(b). Furthermore, Cu

precipitates were found in cementite, as earlier observed in other materials [34–36].

In a study by Oba et al. [37], high resolution material characterisation by neutron scattering experiments was applied to Fe-C-Cu-V alloys. The composition of the samples was Fe-0.04C-1Cu-0.5Ni-0.2 V. Samples were cast and hot-rolled, quenched, and aged at 550°C to form precipitates. This material is different compared to the powder forged material studied in the present work, both in composition (Fe-0.48C-3Cu-0.1 V), and in how it was produced. Still, it is interesting to note that the authors claim to find co-precipitation of Cu and VC in the material, and that V-carbides act as nucleation sites for Cu, since VC precipitates before Cu, in line with what is observed for Cu and VN here. Furthermore, Cu, Ni, and Mn were found to precipitate on VN during long term thermal ageing at 345°C during operation of a pressuriser from Ringhals power plant by Lindgren et al. and Boåsen et al. [13,38]. In this weld metal, the VN was there from the manufacturing of the material, demonstrating VN acting as points of nucleation for the Cu-containing precipitates.

In this paper, undeformed and deformed material tested at both room temperature and 120°C was analysed. From the APT measurements, it is not possible to say anything about a possible difference between M-RT and M-120, due to the local deformation and also the Cu content varying significantly between the analyses. The deformation resulted in modified Cu precipitate characteristics, presumably due to shearing by dislocations. The exact extent of this is believed to be different locally and thus hard to reconstruct after testing, but it was observed that the Cu-Cu RDFs were affected, possibly due to the precipitates becoming sheared in the process. The total volume fraction was not affected, indicating that the precipitates were not dissolved by the process. Furthermore, the testing at a temperature of 120°C, is thus not expected to significantly increase the diffusion rate of Cu, even with the high deformations experienced by the material, as suggested by Ilia et al [3], since there is no increase in cluster volume fraction after testing at elevated temperature. The metal is supersaturated with Cu [39] and if diffusion was possible the Cu precipitate volume fraction would thus increase. However, it is possible that a small contribution from deformation induced diffusion could contribute to the more diffuse particles observed by APT.

The VN clustering appears to be affected by the deformation, as the average V-V RDF(0) is higher for M-ref than for the deformed materials (Figure 9), again interpreted as the precipitates being sheared by the dislocations.

The addition of V was intended to increase the mechanical properties of the material and it indeed improved the room temperature properties. However, at elevated temperatures, the ultimate tensile and yield strength were not significantly increased as expected, when compared to the behaviour of Fe-Cu-C material, see Table 3. The reason for this is currently unknown and requires further testing and analysis of the material.

5. Conclusions

In summary, the investigation of powder forged Fe-V-Cu-C shows that:

- There are Cu precipitates in ferrite, cementite, and in the ferrite/cementite interface
- The Cu precipitate characteristics is very dependent on the local Cu content, which was found to vary between at least 0.8 and 3.5 at.%.
- There are VN precipitates, acting as nucleation points for the Cu precipitates during the cooling of the material.
- The Cu precipitates and VN are more diffuse after tensile testing, possibly from being sheared by dislocations in the process.
- The volume fraction of Cu precipitates is only dependent on the local Cu content, indicating that no significant diffusion of Cu takes place during deformation at room temperature or 120°C.

Acknowledgements

The characterisation of the materials was performed in Chalmers Materials Analysis Lab (CMAL). Höganäs AB is acknowledged for providing the material. Magnus Hörnqvist Colliander at the Department of Physics, Chalmers is acknowledged for fruitful discussions.

Disclosure statement

No potential conflict of interest was reported by the author(s).

ORCID

Kristina Lindgren http://orcid.org/0000-0003-3419-1784
Maheswaran Vattur Sundaram http://orcid.org/0000-0001-5759-8160

References

[1] N. Fraser, H. Blaxill, G. Lumsden and M. Bassett, *Challenges for increased efficiency through gasoline engine downsizing*. SAE Int. J. Engines 2 (2009), pp. 991–1008.
[2] E. Ilia and W. Brian James, *Powder-forged steel*, in *Powder Metallurgy*, P. Samal, J. Newkirk, ed., ASM International, Novelty, OH, 2015. pp. 347–373.
[3] E. Ilia, P. Plamondon, J.-P. Masse and G. L'Espérance, *Copper precipitation at engine operating temperatures in powder-forged connecting rods manufactured with Fe–Cu–C alloys*. Mater. Sci. Eng. A 767 (2019), p. 138383.
[4] H.K.D.H. Bhadeshia and R.W.K. Honeycombe, *Steels Microstructure and Properties*, 3rd ed., Butterworth-Heinemann, Oxford, 2006.
[5] J. Zhu, T. Zhang, Y. Yang and C.T. Liu, *Phase field study of the copper precipitation in Fe-Cu alloy*. Acta Mater. 166 (2019), pp. 560–571.

[6] P.J. Othen, M.L. Jenkins, G.D.W. Smith and W.J. Phythian, *Transmission electron microscope investigations of the structure of copper precipitates in thermally-aged Fe-Cu and Fe-Cu-Ni*. Philos. Mag. Lett. 64(6) (1991), pp. 383–391.
[7] P.J. Othen, M.L. Jenkins and G.D.W. Smith, *High-resolution electron microscopy studies of the structure of Cu precipitates in α-Fe*. Philos. Mag. A 70(1) (1994), pp. 1–24.
[8] S.K. Ghosh, A. Haldar and P.P. Chattopadhyay, *On the Cu precipitation behavior in thermomechanically processed low carbon microalloyed steels*. Mater. Sci. Eng. A 519 (1-2) (2009), pp. 88–93.
[9] E. Ilia, M. O'Neill and K. Tutton, *Higher fatigue strength materials for powder metal forged connecting*. J. Mater. Manuf. 111 (2002), pp. 317–323.
[10] E. Ilia, K. Tutton and M. O'Neill. Impact of copper and carbon on mechanical properties of iron-carbon-copper alloys for powder metal forging applications, US Patent Application No. 11/253,298, 2006.
[11] E. Ilia, *The effect of copper precipitation on mechanical properties at operating temperature of the materials used to manufacture powder forged connecting rods*. Int. J. Powder Metall. 50(4) (2014), pp. 11–20.
[12] M.K. Miller, *Atom Probe Tomography: Analysis at the Atomic Level*, Kluwer Academic/Plenum Publishers, New York, 2000.
[13] K. Lindgren, M. Boåsen, K. Stiller, P. Efsing and M. Thuvander, *Cluster formation in in-service thermally aged pressurizer welds*. J. Nucl. Mater. 504 (2018), pp. 23–28.
[14] V.A. Hosseini, K. Hurtig, D. Gonzalez, J. Oliver, N. Folkeson, M. Thuvander, K. Lindgren and L. Karlsson, *Precipitation kinetics of Cu-rich particles in super duplex stainless steels*. J. Mater. Res. Technol. 15 (2021), pp. 3951–3964.
[15] M.K. Miller and K.F. Russell, *Embrittlement of RPV steels: An atom probe tomography perspective*. J. Nucl. Mater. 371(1-3) (2007), pp. 145–160.
[16] R. Prakash Kolli and D.N. Seidman, *The temporal evolution of the decomposition of a concentrated multicomponent Fe–Cu-based steel*. Acta Mater. 56(9) (2008), pp. 2073–2088.
[17] P.D. Styman, J.M. Hyde, K. Wilford, A. Morley and G.D.W. Smith, *Precipitation in long term thermally aged high copper, high nickel model RPV steel welds*. Prog. Nucl. Energy 57 (2012), pp. 86–92.
[18] R.P. Kolli and D.N. Seidman, *Co-precipitated and collocated carbides and Cu-rich precipitates in a Fe-Cu steel characterized by atom-probe tomography*. Microsc. Microanal. 20(6) (2014), pp. 1727–1739.
[19] M. Thuvander, J. Zhou, J. Odqvist, S. Hertzman and P. Hedström, *Observations of copper clustering in a 25Cr-7Ni super duplex stainless steel during low-temperature aging under load*. Philos. Mag. Lett. 92 (2012), pp. 336–343.
[20] Computational Materials Engineering – Thermo-Calc Software (thermocalc.com).
[21] D.R. Kingham, *The post-ionization of field evaporated ions: A theoretical explanation of multiple charge states*. Surf. Sci. 116 (1982), pp. 273–301.
[22] J.M. Hyde and C.A. English, *An analysis of the structure of irradiation induced Cu-enriched clusters in low and high nickel welds*, Materials Research society symposium, vol. 650, Boston, 2000, pp. R6.6.1–R6.6.12.
[23] D. Vaumousse, A. Cerezo and P.J. Warren, *A procedure for quantification of precipitate microstructures from three-dimensional atom probe data*. Ultramicroscopy 95 (2003), pp. 215–221.
[24] E.A. Marquis, V.J. Araullo-Peters, Y. Dong, A. Etienne, S. Fedotova, K. Fujii, K. Fukuya, E. Kuleshova, A. Lopez, A. London, S. Lozano-Perez, Y. Nagai, K. Nishida, B. Radiguet, D.K. Schreiber, N. Soneda, M. Thuvander, T. Toyama, F. Sefta and P. Chou, *On the use of density-based algorithms for the analysis of solute clustering in*

atom probe tomography data, 18th International Conference on Environmental Degradation of Materials in Nuclear Power Systems – Water Reactors. The Minerals, Metals & Materials Series, Springer, 2017, pp. 2097–2113.

[25] Y. Dong, A. Etienne, A. Frolov, S. Fedotova, K. Fujii, K. Fukuya, C. Hatzoglou, E. Kuleshova, K. Lindgren, A. London, A. Lopez, S. Lozano-Perez, Y. Miyahara, Y. Nagai, K. Nishida, B. Radiguet, D.K. Schreiber, N. Soneda, M. Thuvander, T. Toyama, J. Wang, F. Sefta, P. Chou and E.A. Marquis, *Atom probe tomography inter-laboratory study on clustering analysis in experimental data using the maximum separation distance approach*. Microsc. Microanal. 25(2) (2019), pp. 356–366.

[26] K. Lindgren, K. Stiller, P. Efsing and M. Thuvander, *On the analysis of clustering in an irradiated low alloy reactor pressure vessel steel weld*. Microsc. Microanal. 23(2) (2017), pp. 376–384.

[27] O.C. Hellman, J.A. Vandenbroucke, J. Rüsing, D. Isheim and D.N. Seidman, *Analysis of three-dimensional atom-probe data by the proximity histogram*. Microsc. Microanal. 6(5) (2000), pp. 437–444.

[28] M.K. Miller and R.G. Forbes, *Atom-Probe Tomography: The Local Electrode Atom Probe*, Springer, New York, 2014.

[29] C.P. Wang, X.J. Liu, I. Ohnuma, R. Kainuma and K. Ishida, *Phase equilibria in Fe-Cu-X (X: Co, Cr, Si, V) Ternary systems*. J. Phase Equilib. 23 (2002), pp. 236–245.

[30] E.M. Savitskii, V.V. Baron and Y.V. Efimov, *Investigation of vanadium-copper-carbon and vanadium-copper- aluminium alloys*. Metall. Metallogr. Phys.-Chem. Invest. Methods 9 (1996), pp. 120–127.

[31] Thermo-Calc, Computational Materials Engineering – Thermo-Calc Software (thermocalc.com) – Precipitation Module (TC-PRISMA) User Guide, Thermo-Calc Version 2021b 2021. https://thermocalc.com/content/uploads/Documentation/Current_Static/precipitation-module-tc-prisma-user-guide.pdf.

[32] C-N-V Isothermal Section of Ternary Phase Diagram 2016. Available at https://materials.springer.com/isp/phase-diagram/docs/c_0207670 (Accessed 2021-11-30).

[33] R.T. Warzel III, B. Hu, A. Tims and M. Milligan, *The effect of sintering conditions on the mechanical properties of prealloyed vanadium powder metallurgy steels*. Int. J. Powder Metall. 55 (2019), pp. 31–37.

[34] J. Zelenty, G.D.W. Smith, K. Wilford, J.M. Hyde and M.P. Moody, *Secondary precipitation within the cementite phase of reactor pressure vessel steels*. Scr. Mater. 115 (2016), pp. 118–122.

[35] F.A. Khalid and D.V. Edmonds, *On the properties and structure of micro-alloyed and copper-bearing hot-rolled steels*. J. Mater. Process. Technol. 72 (1997), pp. 434–436.

[36] F.A. Khalid and D.V. Edmonds, *A transmission electron microscopy study of copper precipitation in the cementite phase of hypereutectoid alloy steels*. Metall. Trans. A 24 (1993), pp. 781–793.

[37] Y. Oba, S. Morooka, H. Sato, N. Sato, K. Ohishi, J.-i. Suzuki and M. Sugiyama, *Simultaneous characterisation of precipitates and matrix in a steel using small-angle neutron scattering and bragg-edge transmission analysis*. ISIJ Int. 55(12) (2015), pp. 2618–2623.

[38] M. Boåsen, K. Lindgren, M. Öberg, M. Thuvander, J. Faleskog and P. Efsing, *Analysis of thermal embrittlement of a low alloy steel weldment using fracture toughness and microstructural investigations*. J. Nucl. Mater. 262 (2022), pp. 108248.

[39] W.F. Gale and T.C. Totemeier, eds. *Smithells Metals Reference Book*, 8th ed., Elsevier, Oxford, 2004.